# Alkali-cation-incorporated and functionalized iron oxide nanoparticles for methyl blue removal/decomposition

**PAPER • OPEN ACCESS**

# Alkali-cation-incorporated and functionalized iron oxide nanoparticles for methyl blue removal/decomposition

To cite this article: N Joseph Singh *et al* 2020 *Nanotechnology* **31** 425703

View the article online for updates and enhancements.

## Recent citations

- Co-pyrolysis of cyanobacteria and plastics to synthesize porous carbon and its application in methylene blue adsorption
Lixin Li *et al*

# Alkali-cation-incorporated and functionalized iron oxide nanoparticles for methyl blue removal/decomposition

**N Joseph Singh**[1]**, Boris Wareppam**[1]**, Subrata Ghosh**[2]📷**, B Prasad Sahu**[3]**, P K AjiKumar**[4]**, H Premjit Singh**[5]**, Soumee Chakraborty**[4]**, S S Pati**[6]**, A C Oliveira**[7]**, Suelen Barg**[2]📷**, V K Garg**[7] **and L Herojit Singh**[1]

[1] Department of Physics, National Institute of Technology Manipur, Langol, Imphal 795004, India
[2] Department of Materials, School of Natural Sciences, The University of Manchester, Oxford Road, Manchester M13 9PL, United Kingdom
[3] Department of Metallurgical and Materials Engineering, Indian Institute of Technology, Kharagpur 721302, India
[4] Materials Science Group, Indira Gandhi Centre for Atomic Research, Kalpakkam 603102, India
[5] Process Control & Analytical Laboratory, Heavy Water Board (Manuguru), Department of Atomic Energy, Telangana 507116, India
[6] Department of Chemistry, National Institute of Technology Jamshedpur, Jharkhand 831014, India
[7] Institute of Physics, University of Brasília, 70919-970, Brasília, DF, Brazil

E-mail: subrataghosh.phys@gmail.com, subrata.ghosh@manchester.ac.uk, herojit@nitmanipur.ac.in and loushambam@gmail.com

## Abstract

Enhancing the rate of decomposition or removal of organic dye by designing novel nanostructures is a subject of intensive research aimed at improving waste-water treatment in the textile and pharmaceutical industries. Despite radical progress in this challenging area using iron-based nanostructures, enhancing stability and dye adsorption performance is highly desirable. In the present manuscript alkali cations are incorporated into iron oxide nanoparticles (IONPs) to tailor their structural and magnetic properties and to magnify methyl blue (MB) removal/decomposition capability. The process automatically functionalizes the IONPs without any additional steps. The plausible mechanisms proposed for IONPs incubated in alkali chloride and hydroxide solutions are based on structural investigation and correlated with the removal/adsorption capabilities. The MB adsorption kinetics of the incubated IONPs is elucidated by the pseudo second-order reaction model. Not only are the functional groups of –OH and –Cl attached to the surface of the NPs, the present investigation also reveals that the presence of alkali cations significantly influences the MB adsorption kinetics and correlates with the cation content and atomic polarizability.

Keywords: iron oxide nanoparticles, structural properties, surface modification, dye adsorption, waste-water treatment

(Some figures may appear in colour only in the online journal)

## 1. Introduction

The enormous quantities of waste water produced every year due to the extensive use of organic dyes in the pharmaceutical, food, rubber, pesticide, cosmetic and textile industries are a great threat to the environment [1–3]. The dyeing of

garments and subsequent treatment processes use significant amounts of harmful chemicals and dyes which produce huge quantities of toxic organic matter and heavy metals, such as zinc, copper, lead, cadmium, etc, as by-products [4, 5].

Methyl blue ($C_{37}H_{27}N_3Na_2O_9S_3$) is one such commonly used dye that is toxic and nonbiodegradable, and its release into the environment causes severe destruction of the aquatic ecosystem, increasing the chemical/biological oxygen demand of water bodies and reducing light penetration and affecting photosynthesis. It is highly visible and undesirable even when a small amount of dye is present and poses a serious threat to the human population due to mutagenic and carcinogenic effects [6, 7]. Therefore, the elimination/decomposition of dyes from waste water as well as proper disposal routes are highly necessary.

Nanotechnology is anticipated to play a huge role in water decontamination and purification [8]. Among the adoptable strategies, adsorption/decomposition is one of the most promising, highly effective and inexpensive techniques to remove dyes from waste water [9]. Moreover, the efficient adsorption/decomposition of these toxic elements from waste water by adsorbents makes this technique quite feasible. Therefore, the search for appropriate adsorbents or catalysts is receiving significant attention.

In the context of methyl blue (MB) adsorption, the library of materials with extensively registered interest includes graphene-based materials [10, 11], metal oxides [12–14] and their composites [15, 16] due to their remarkable properties in the nanoscale dimension. Despite this, iron-oxide-based nanostructures (IONSS) have received significant interest as a potential adsorbent/catalyst owing to the natural occurrence of IOs and simple methods of preparation, diverse adsorption features to remove the contaminants, the fast adsorption rate, the presence of functional groups which interact easily with the waste compounds, higher reduction ability in $NO^{3-}$ to $NO^{2-}$, their nontoxic nature, higher environmental stability and feasible reusability by desorption processes [17–20]. IONSS can be easily dispersed in a solution for purification, and due to their magnetic nature, the dispersed nanoparticles (NPs) can be separated simply by using a magnet. Moreover, these magnetic NPs permit faster magnetic separation from the adsorbate. Additionally, to further enhance MB adsorption, several strategies can be adopted. While $Fe_3O_4$ nanopowder shows an MB adsorption capacity of 86.63%, the performance is further enhanced by making a composite with reduced graphene oxide (MB adsorption capacity increased to 95.32%) [19]. While the design of an IO-based composite has gained much attention for enhancing the MB adsorption property, much less attention has been paid to the surface modification of IO itself.

Apart from studying bare IONSs, the role of the –OH functional groups of the dyes on adsorption ability at the surface of IONPs has been studied extensively [20]. It has been shown that the –OH functional groups can bind better with IONPs than others, which leads to enhanced adsorption capacity [20]. However, the surface interactions of cations with IONPs in various environments in a colloidal solution and the

effect on MB adsorption are yet to be investigated. The present study gives an insight into the mechanisms of dye removal by IONPs.

While synthesizing cation-incorporated and functionalized IONPs is the main goal for current research, in the main, the natural co-existence of different phases of IO poses the biggest challenge to synthesizing IO with a single phase. Hematite ($\alpha$–$Fe_2O_3$), magnetite ($Fe_3O_4$) and maghemite ($\gamma$–$Fe_2O_3$) are the most common phases of IO in nature, with widespread applications in the field of catalysis, optoelectronics, spintronics, sensors, magnetic recording media, energy storage and magnetic fluid heating applications [21–27]. Amongst these oxides, $Fe_3O_4$ and $\gamma$–$Fe_2O_3$ possess similar structures and magnetic properties, except for the difference in $Fe^{2+}$ vacancies [21]. While mixed oxides exhibit synergetic features [28], it would be interesting to examine the dye adsorption capabilities of mixed oxides from the same cation, $Fe_3O_4/\gamma$–$Fe_2O_3$. Moreover, the structural stability of the as-synthesized IONPs is a major concern. $\gamma$–$Fe_2O_3$ NPs with a tailored size (2–7 nm), synthesized using NaOH as a base for precipitation, are reported to have higher stability than those precipitated using $NH_3$ solution, while also showing the ability to retain their ferrimagnetic structure up to 700 °C [29].

The importance of choosing an appropriate medium during IONP synthesis is also crucial to improving their structural stability. It is also proposed that alkali cations reside in the crystal lattice as the crystal nucleates. Unfortunately, regarding the kinetics of the cation's interaction with the NPs, it is not yet understood whether the alkali cations get trapped during the nucleation of the magnetite NPs or diffuse into the lattice of the NPs after nucleation. On the other hand, the replacement of Fe cations by $Li^+$ ions leads to enhanced stability beyond 1000 °C [30]. Moreover, magnetic IONPs possess the property of being able to adsorb cations, which allows heavy cations to separate from the solution by adsorption on the surface of the NPs [31].

With the above-mentioned background, the present research is divided into two. The first part focuses on the synthesis of cation-decorated IONPs in different colloidal solutions, namely, alkali chloride and hydroxide by co-precipitation methods. The second one is to explore the plausible mechanisms of cation incubation for IONPs in various environments and its influence on their physico-chemical, structural, vibrational and magnetic properties. The consequences of the first part are extended to the impact of these simultaneous cation-induced and functionalized IONPs on MB adsorptions/decompositions.

## 2. Materials and methods

### 2.1. Materials

MB, $FeSO_4.7H_2O$, LiOH, KOH, LiCl, NaCl and KCl were purchased from Himedia India. $FeCl_3$, NaOH and 25 wt% $NH_3$ were purchased from Fisher Scientific India, Merck India and Sisco Research Laboratories India with purity above 98%, respectively. All analytical grade chemicals were used as received without further purification. Distilled water (Quarts

Bi-distillation unit, Borosil India) was used to prepare the aqueous solutions.

## 2.2. Synthesis method

Bare IONPs were synthesized using the co-precipitation method. Briefly, 50 ml of 1 M $FeSO_4.7H_2O$ was mixed with 50 ml of 2 M $FeCl_3$ aqueous solution and magnetically stirred for 40 min at 70 °C. Thereafter, 25 wt% $NH_3$ was added to the above iron-based solution under vigorous stirring to maintain the pH at ~11 for 1 h. Once the solution was cooled to room temperature, the NPs were washed several times with double-distilled water. An equal amount of precipitate (400 mg) was incubated in various alkali solutions (0.5 M of chloride and hydroxides of Li, Na and K). Finally, the products were washed and dried at a temperature of 60 °C for 8 h. The as-synthesized NPs are marked as *M*. The NPs incubated in alkali chlorides and hydroxides are marked as *M–X*Cl and *M–X*OH respectively, where *X* represents Li, Na and K.

## 2.3. Characterizations

Transmission electron microscopy (TEM) images of IONPs were obtained by using a microscope (JEOL, India) to determine the morphology and the particle size distribution. The phase and crystallographic information of the IONPs were evaluated using x-ray diffraction (XRD) (Bruker-D8 advance, USA) with Cu $K_\alpha$ radiation of wavelength 1.54056 Å.

A Fourier transform infrared spectrometer (FTIR) (Perkin Elmer, USA) and a micro-Raman spectrometer (inVia Renishaw, UK) were employed to investigate the vibrational properties of the studied NPs. To record the Raman spectra of IONPs, a 514 nm LASER was used with a 50 × objective lens and the laser power was kept below 1 mW to avoid laser-induced heating of the sample. The infrared spectra were recorded using a KBr beam splitter. $Fe^{57}$ Mössbauer spectroscopy was utilized in transmission mode with an initial activity of 25 mCi (Wissel, Germany).

Thermo-gravimetric analysis (TGA) and differential thermal analysis (DTA) were carried out by a thermogravimetric analyzer (SETSYS 16/18, SETARAM-France) equipped with a high-temperature furnace. All NPs were taken in alumina crucibles and subjected to a heating rate of 10 K $min^{-1}$ from 300 K to 1273 K in an $Ar/O_2$ gas atmosphere.

The alkali content of the NPs was determined using ICPMS (Inductively Coupled Plasma Mass spectrometry), a home-built set up from the Bhabha Atomic Research Centre (BARC), India. The MB adsorption was performed using UV–vis spectrometer (Shimadzu-1800, Japan).

## 3. Results and discussions

### 3.1. Morphology and structural analysis

The morphology of the as-synthesized IONPs was examined by direct observation via TEM and a representative TE micrograph is displayed in figure 1(a). The micrograph confirms the

nearly spherical shape of the IONPs with an average size of 12 nm (inset of figure 1(a)). As shown in the selected area electron diffraction (SAED) pattern (figure 1(b)), the prepared NPs confirm the formation of a polycrystalline cubic iron oxide ($Fe_3O_4$) phase.

To identify the phase further, XRD was performed and the corresponding diffractograms of bare NPs (*M*), *M–X*Cl and *M–X*OH are presented in figure 1(c). All samples studied here reveal an almost similar XRD with the lattice planes at (220), (311), (400), (611) and (440), which is in good agreement with the SAED pattern. The result again confirms the cubic phase ($Fe_3O_4$) of the iron oxide structure (JCPDS card no. 19–0629). The calculated lattice parameter of the as-synthesized NPs (*M*) is ~0.834 nm, which is close to that of magnetite (0.833 nm) and maghemite (0.834 nm) [32]. The average size of the NPs is estimated using the Debye–Scherrer formula and found to be ~9 ± 2 nm, which matches well with the histogram result (inset of figure 1(a)).

The obtained result was certainly not sufficient to identify the phase of the cubic IONPs among the maghemite and magnetite. In other words, the synthesized NPs may have had both phases, and hence spectroscopic investigations were carried out.

### 3.2. Spectroscopic investigations

Attenuated total reflection FTIR spectroscopy was used to investigate the vibrational bands and functional groups both before and after adsorption of alkali ions on the surfaces of the IONPs. The samples (*M, M–X*Cl and *M–X*OH) exhibit an intense peak around 540 $cm^{-1}$ which is attributed to the stretching vibration associated with the metal–oxygen (Fe–O) bonds in the crystalline lattice of magnetite/maghemite (see figure 2) [33]. This peak at 540 $cm^{-1}$ is characteristically pronounced for all spinel structures, particularly ferrites. Besides this, other prominent absorptions were obtained at wavenumbers 1061, 1347, 1597 and 3300 $cm^{-1}$ for bare NPs (*M*). The absorption peaks for *M–X*Cl and *M–X*OH are observed at ~1061, 1340, 1603–1629 and 3300 $cm^{-1}$. The peak located at ~1061 $cm^{-1}$ arises from symmetric C–O stretching for the monodentate structures of carbonates. The peaks located at ~1340 and 1600 $cm^{-1}$ are assigned to the C–O–O– symmetric stretching and C–O–O– asymmetric stretching of the adsorbed bicarbonates, respectively [34]. The presence of C–O and C–O–O may be understood due to $CO_2$ adsorption from the open atmosphere [34]. There are noticeable changes in the intensity of the C–O–O– asymmetric stretching mode for the *M*–LiCl and *M*–NaCl, and a shift in position towards a higher wavenumber by 6 to 32 $cm^{-1}$ compared to that of the bare NPs is also observed (see figure 2(a)). Similar to the *M–X*Cl, enhanced peak intensities in both C–O–O– symmetric and asymmetric modes are observed for *M*–NaOH and *M*–KOH incubation (see figure 2(b)). In the case of *M–X*Cl and *M–X*OH, the position of the C–O–O– asymmetric stretching vibrational mode shifted towards a higher wavenumber by 2 to 28 $cm^{-1}$ and a lower wavenumber by 8 to 12 $cm^{-1}$ compared to the bare NPs, respectively.
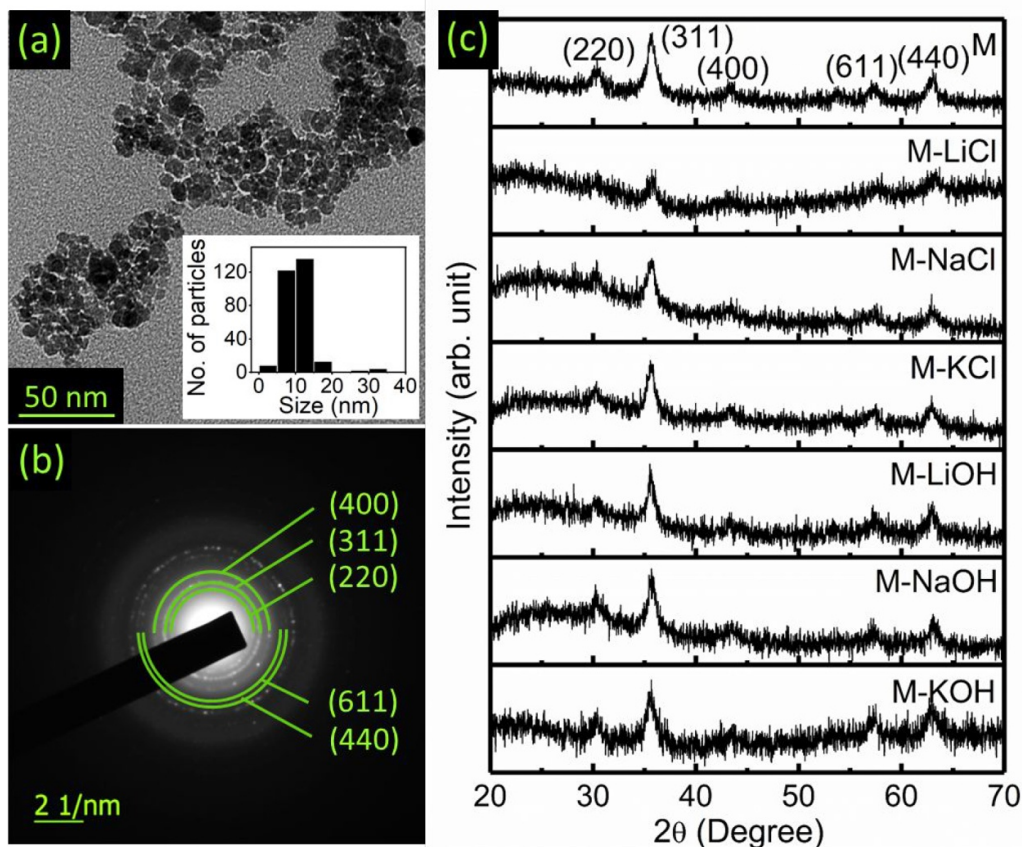
**Figure 1.** (a) The transmission electron micrograph and inset represent the histogram of distribution and (b) the SAED pattern of cubic iron oxide nanoparticles; (c) the XRD of bare iron oxide (*M*) and iron oxide incubated in alkali chloride (*M*–*X*Cl) and hydroxide (*M*–*X*OH) nanoparticles.
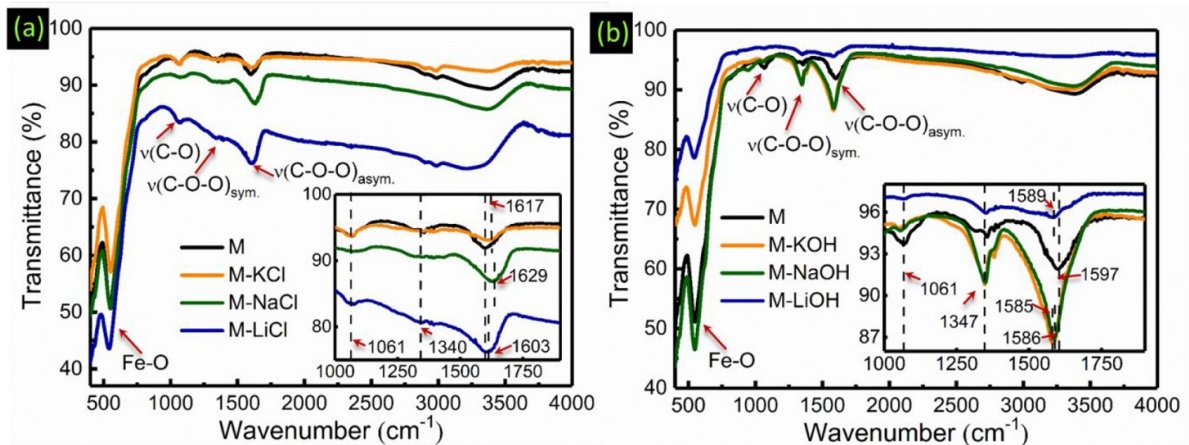


**Figure 2.** The FTIR spectra of (a) *M*–*X*Cl and (b) *M*–*X*OH along with bare nanoparticles (*M*); *X* = Li, Na, K.

These observations can be interpreted as follows: (i) the nature of cations (Li$^+$, Na$^+$ or K$^+$) has a significant influence on the functional group attached to the surface of the IONPs after incubation; (ii) the incubation mechanism of alkali chlorides and alkali hydroxides into the IONPs is not the same. Further investigations of the vibrational properties of alkali-cation-incubated IONPs are carried out using Raman spectroscopy.

The Raman scattering of iron oxides has been the subject of numerous investigations attempting to obtain a deeper understanding of the structure [35]. The Raman spectra of the samples are divided into two parts: 200–800 cm$^{-1}$, which represents the vibrations related to iron oxide, and 800–2000 cm$^{-1}$ containing overlapped modes from iron-oxide and carbon-related structures (see figure 3).
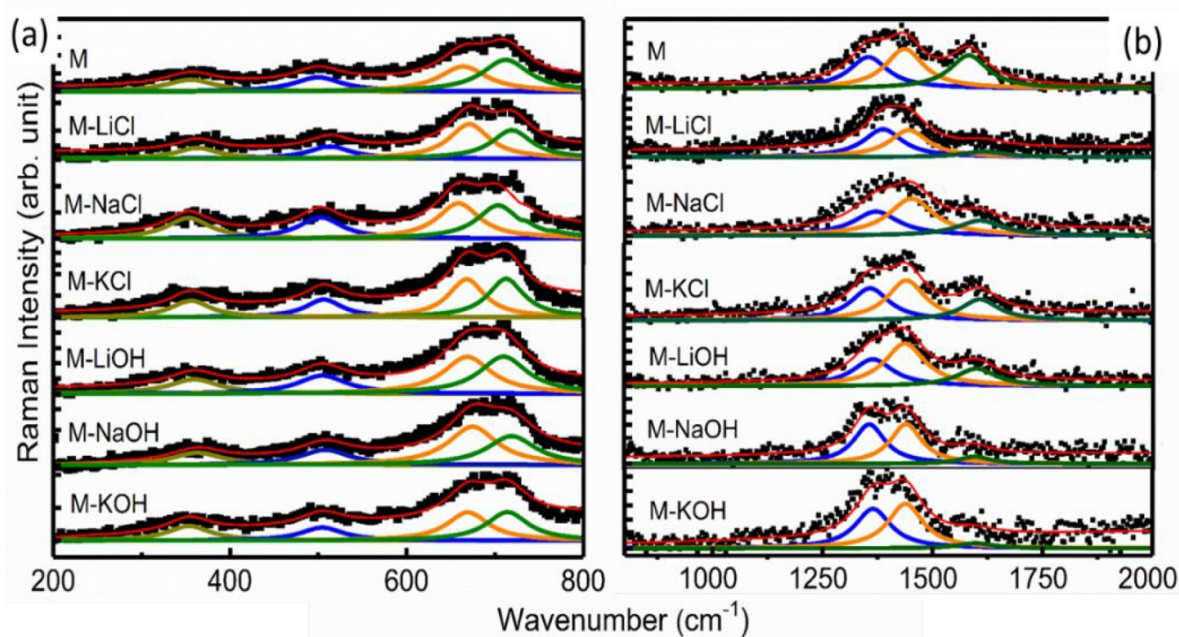
**Figure 3.** The Raman spectra of bare IONPs (*M*), *M*–*X*OH and *M*–*X*Cl in the (a) the 200–800 cm$^{-1}$ and (b) the 800–2000 cm$^{-1}$ range. (*X* represents Li, Na and K.)

The first-order Raman spectra are fitted with Lorentzian line shapes which exhibit the most prominent features ~360, 500, 675 and 720 cm$^{-1}$ (see figure 3(a)). With a spinel structure (O$^7_h$), magnetite (Fe$_3$O$_4$) shows five Raman bands: three T$_{2\,g}$ (~193, 450–490 and 538 cm$^{-1}$), one E$_g$ ~306 cm$^{-1}$ and one A$_{1\,g}$ at around 668 cm$^{-1}$ [36]. It is also reported that three broad bands ~350, 500 and 700 cm$^{-1}$ are generally assigned as T$_{2\,g}$, E$_g$ and A$_{1\,g}$ respectively, for maghemite [37, 38]. Hanesch [39] reported the presence of Raman bands at ~350, 512, 664 and 726 cm$^{-1}$ in the maghemite phase of iron oxide. The Raman modes at 365 (T$_{2\,g}$), 511 (E$_g$) and 700 (A$_{1\,g}$) were also assigned to maghemite [35]. The Raman bands of maghemite are generally broadened and shifted to higher energies compared to that of the magnetite [40]. Two modes observed here in the cubic IO phase ~675 and 720 cm$^{-1}$ are approximately in agreement with the A$_{1\,g}$ modes as reported by Silva *et al* [41]. The vibrational mode at higher energy with A$_{1\,g}$ symmetry is associated with the stretching vibrational mode of the Fe$^{3+}$ ions in tetrahedral (A) sites surrounded by four nearest O$^{2-}$ ions, where each one is bounded to the nearest octahedral (B) sites occupied by twelve Fe$^{3+}$/Fe$^{2+}$ ions (Fe$^A$–O$_4$–Fe$^B_{12}$). The oxidation from Fe$^{2+}$ to Fe$^{3+}$ in magnetite results in the formation of maghemite which leads to cation deficient B-sites (Fe$_A$–O$_{4-}$(Fe$_8$□$_4$)$_B$), where □ represents the cationic vacancies responsible for the shift in the Raman peak from 675 to 720 cm$^{-1}$. Hence, the peak ~675 cm$^{-1}$ obtained in all studied samples is one of the characteristic peaks of magnetite and the peak around 720 cm$^{-1}$ arises due to maghemite formation.

The above facts reveal that both magnetite and maghemite structures are present in all the IONP samples synthesized in the present study. Hence, it will be interesting to estimate the magnetite/maghemite ratio to investigate the influence

**Table 1.** The fitted positions of A$_{1\,g}$ modes corresponding to magnetite and maghemite with the magnetite/maghemite intensity ratio.

| Samples | A$_{1\,g}$ modes of magnetite (cm$^{-1}$) | A$_{1\,g}$ modes of maghemite (cm$^{-1}$) | Magnetite/ Maghemite |
|---|---|---|---|
| *M* | 665 | 711 | 0.93 |
| *M*–LiOH | 665 | 707 | 0.99 |
| *M*–NaOH | 671 | 716 | 1.33 |
| *M*–KOH | 669 | 714 | 1.12 |
| *M*–LiCl | 667 | 716 | 1.20 |
| *M*–NaCl | 666 | 712 | 1.06 |
| *M*–KCl | 663 | 709 | 0.99 |

of alkali cations incorporated into the IONPs by taking the integrated areas associated with 675 and 720 cm$^{-1}$ modes [35, 41]. The magnitude of oxidation along with the peak positions of A$_{1\,g}$ modes of all the samples is presented in table 1. It is observed that the relative amount of magnetite is higher in the alkali- cation-incorporated IONPs compared to that of the bare NPs. It may be inferred that the alkali cations adsorbed by the NPs shield the Fe cations of IO from the environment and prevent oxidation.

To probe further the alkali-cation-induced enhancement for the relative amount of magnetite/maghemite in the IONPs, the Raman spectra of samples in the range 800–2000 cm$^{-1}$ are deconvoluted (see figure 3(b)). The deconvolution results in three peaks at ~1350, 1450 and 1620 cm$^{-1}$. Within this range, the main characteristic peaks of the defected nanocarbons are the D peak at around 1350 cm$^{-1}$, the G peak around 1580 cm$^{-1}$ and the D′ peak at 1620 cm$^{-1}$ [42]. Because the

zone in this region overlaps those of the characteristic peaks of carbon-related materials [38], analysis of the high-frequency Raman spectra of IONPs is generally ignored. FTIR inspection on the IONPs, as discussed before, suggests $CO_2$ adsorption from the open atmosphere and the prominent intensity enhancement of specific vibrational modes is a signature of the influence of alkali cations on the IONPs. However, it is obvious that $CO_2$ adsorption on the IONPs is not sufficient to form any iron carbide or iron-oxide–carbon composites. Thus, the peaks around 1350, 1450 and 1620 $cm^{-1}$ may be attributed to the genuine intrinsic vibrational features of IONPs. The peak at ~1350 $cm^{-1}$ is assigned to the magnon mode of iron oxide [43, 44]. It is also reported that maghemite exhibits intense and sharp vibrational modes ~1450 and 1620 $cm^{-1}$ whereas the Raman signal around 1600 $cm^{-1}$ is absent in magnetite [35]. Thus, it is confirmed that all IONPs are dominated by maghemite structures, but a relative amount of magnetite is found to increase upon the incorporation of alkali cations.

### 3.3. Mössbauer analysis

[57]Fe Mössbauer spectrometry is highly sensitive to superparamagnetic relaxation phenomena and as a result, it is a very powerful technique for studying the dynamics of magnetic nanostructures [45, 46]. The variation of Mössbauer parameters, viz. isomer shift, quadrupole splitting, area and the hyperfine field of IONPs after incubation with alkali chloride and hydroxide are expected to provide more insights into the kinetics of alkali cations. Figure 4(a) shows the [57]Fe Mössbauer spectra measured at room temperature. Each spectrum is fitted with two sextets corresponding to the tetrahedral and octahedral Fe, one sextet corresponding to the disordered spins of Fe atoms residing at the surface of the nanoparticles and one doublet indicating that the Fe atoms experience superparamagnetism.

The hyperfine parameters derived from the spectra are listed in table 2. The spectrum of the bare IONPs (*M*) consists of three sub-spectra corresponding to the Fe atoms at tetrahedral sites experiencing a hyperfine field of 45.81 T with an area of 34%, octahedral sites (41.30 T and 21%) and the disordered surface spins of Fe[57] (34.9 T and 44%) [47]. The value of Fe is higher at tetrahedral sites than octahedral sites, which is in correlation with the higher content of maghemite as indicated by Raman studies.

The area under the tetrahedral component and subsequent higher octahedral component is observed to be lower for the *M*–*X*Cl than that of the bare NPs, as reflected in the areal contributions (table 2) [48]. This shows that the magnetite content increases after alkali chloride incubation, which is well-supported by the Raman studies (table 1). In the case of *M*–*X*OH, the area for the tetrahedral sites is higher than that of the octahedral except for *M*–LiOH. It is also observed that the spectrum of *M*–LiOH is found to have a higher octahedral component than the tetrahedral, with a similar content of disordered spins of Fe atoms at the surface to that of bare NPs (*M*).

**Table 2.** The list of fitted hyperfine parameters, i.e. area, isomer shift, magnetic field (hyperfine splitting) and quadrupole splitting of bare iron oxide (*M*), *M*–*X*Cl, and *M*–*X*OH.

| Sample | IS (mm s$^{-1}$) | QS (mm s$^{-1}$) | BHF (T) | Area (%) |
|---|---|---|---|---|
| *M* | 0.33 (3) | 0.00 (2) | 45.81(2) | 34 (2.6) |
| | 0.36 (2) | 0.02 (4) | 41.30(6) | 21 (1.8) |
| | 0.44 (5) | 0.11 (7) | 34.9 (1) | 44 (3.2) |
| *M*–LiCl | 0.30 (0) | 0.02 (2) | 46.49(8) | 30 (0.7) |
| | 0.30 (0) | 0.02 (2) | 41.62(6) | 36 (1.7) |
| | 0.35 (6) | 0.11 (7) | 34.90(7) | 34 (2.5) |
| *M*–NaCl | 0.28 (0) | 0.05 (3) | 46.56(2) | 29 (2.0) |
| | 0.33 (0) | 0.04 (5) | 41.40(0) | 34 (10) |
| | 0.42 (7) | 0.02 (9) | 33.20(1) | 37 (2.6) |
| *M*–KCl | 0.31 (1) | −0.06 (3) | 46.54(3) | 29 (2.6) |
| | 0.31 (2) | −0.05 (4) | 42.05(2) | 34 (2.2) |
| | 0.35 (0) | −0.05 (5) | 36.11(7) | 37 (2.2) |
| *M*–LiOH | 0.30 (1) | −0.00 (2) | 46.43(1) | 23 (1.2) |
| | 0.33 (2) | −0.08 (3) | 41.89(4) | 31 (2.3) |
| | 0.32 (0) | −0.01 (5) | 34.00(0) | 46 (2.9) |
| *M*–NaOH | 0.30 (0) | 0.02 (2) | 46.36(1) | 22 (1.1) |
| | 0.30 (0) | 0.12 (2) | 41.18(8) | 21 (1.4) |
| | 0.40 (0) | 0.04 (0) | 34.52(8) | 57 (3.1) |
| *M*–KOH | 0.27 (3) | 0.01 (5) | 45.34(6) | 22 (4.9) |
| | 0.36 (4) | 0.00 (0) | 41.73(6) | 14 (7.2) |
| | 0.30 (4) | 0.06 (6) | 35.87(8) | 64 (7.7) |

Unlike *M*–*X*Cl and *M*–LiOH, the hyperfine parameters of *M*–KOH and *M*–NaOH exhibit a huge deviation. The spectrum under the Fe atoms having disordered spins residing at the surface increases to ~64%. The increase in area of the disordered spins of Fe atoms can be understood due to the reduction in net magnetic moments and dipole–dipole interactions. Basically, adsorbed alkali cations reduce the net magnetic moments of the IONPs, which reduces the dipole–dipole interaction among the particles. Therefore, the reduction in magnetic interaction between the NPs is accomplished for a mean hyperfine field that is lower for *M*–*X*OH than the bare NPs. The mean hyperfine fields ($<B_{hf}>$) of bare and alkali-cation-incubated IONPs are shown in figures 4(b)–(c) for clear visualization. The mean hyperfine field of *M*–*X*Cl is higher than that of the bare IONPs. This may be due to the alkali cations enhancing the dipole–dipole interaction. This is plausible only when the alkali cations reside on the surface and do not affect the net dipole moment but decrease the inter-particle distances.

Therefore, the Mössbauer analysis supports well the FTIR and Raman interpretation that the incubation mechanism of alkali cations into IONPs is certainly different and found to depend on the solvent media (hydroxide or chloride). Further investigation is carried out by TGA-DTA for the possible stability of the Fe matrix with the proposed residence of alkali cations on the surface of the particle.

### 3.4. Structural stability

Since the alkali cations change the physical and chemical properties of IONPs impressively after their incubation, TGA-DTA is imperative for investigating the structural information.
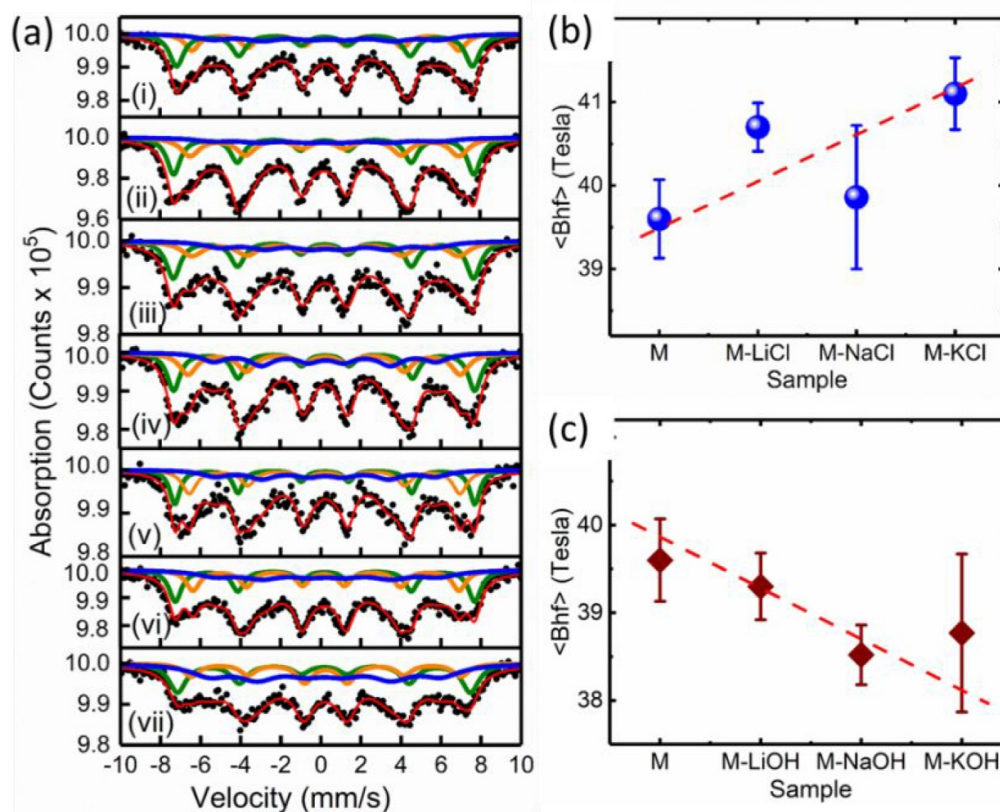
**Figure 4.** (a) The Mossbauer spectroscopy of iron oxide NPs ((i) *M*; (ii) *M*–LiCl; (iii) *M*–NaCl; (iv) *M*–KCl; (v) *M*–LiOH; (vi) *M*–NaOH; (vii) *M*–KOH); the mean hyperfine field ($<B_{hf}>$) of (b) *M*–XCl, and (c) *M*–XOH with that of bare nanoparticles (*M*). (The dashed lines are guides to the eye.)

The TGA-DTA of all incubated samples is shown in figure 5. The weight loss at 400 K for the bare IONPs and NPs incubated in NaCl and KCl is ~5.4%. Surprisingly, the weight loss is ~9.1% for *M*–LiCl which may be the subject of further investigations. The total weight loss of the *M*–*K*OH, *M*–*Na*OH and *M*–*Li*OH are 7.5, 7.45 and 8.4% respectively, which is a bit higher than the bare IONPs.

The key findings from DTA analysis are the different $H_2O$ desorption temperature and structural transition temperatures for *M*–XCl and *M*–XOH as discussed below. The DTA of the NPs shows the presence of two prominent peaks: (i) endothermic, around 400 K, due to the desorption of $H_2O$ molecules from the surface of the NPs and (ii) exothermic, around 843 K, attributed to the structural transition of cubic iron oxides to $\alpha$–$Fe_2O_3$. The desorption temperatures of $H_2O$ molecules for *M*–LiCl and *M*–NaCl are lower than that of bare NPs, whereas that of *M*–KCl is almost the same with its bare counterpart. Besides this, the structural transition temperatures for *M*–XCl are found to be lower than that of bare IONPs (see table 3). This result indicates that alkali cations in the chloride solution are adsorbed only on the surface, meaning extra stabilizing energy could not be provided for the lattices of oxygen and Fe, which would have increased the transition temperature. On the other hand, the desorption temperature of $H_2O$ molecules from the surface of *M*–XOH is observed to be higher by ~8 K–12 K as compared to the

**Table 3.** Weight loss, $H_2O$ desorption and structural transition temperature of *M*, *M*–XCl and *M*–XOH; X = Li, Na, K.

| Sample (0.5 M) | Weight loss (%) | $H_2O$ desorption temperature (K) | Structural transition temperature (K) |
|---|---|---|---|
| *M* | 5.4 | 398 | 841 |
| *M*–LiCl | 9.1 | 396 | 831 |
| *M*–NaCl | 5.4 | 391 | 837 |
| *M*–KCl | 5.4 | 402 | 835 |
| *M*–LiOH | 8.4 | 410 | 850 |
| *M*–NaOH | 7.45 | 406 | 940 |
| *M*–KOH | 7.5 | 409 | 915 |

bare NPs (see table 3). This may be due to the higher binding energy with the surface of the NPs as modified in a basic medium [49]. Unlike that of *M*–XCl and *M*–LiOH, *M*–NaOH and *M*–KOH have three steps of desorption at temperatures around 410 K, 544 K and 641 K. The three steps of desorption may be attributed to the three different binding sites with $H_2O$ molecules [49]. The structural transition temperatures for the NPs incubated in LiOH, NaOH and KOH are increased by 9 K, 97 K and 77 K respectively as compared to the bare NPs.
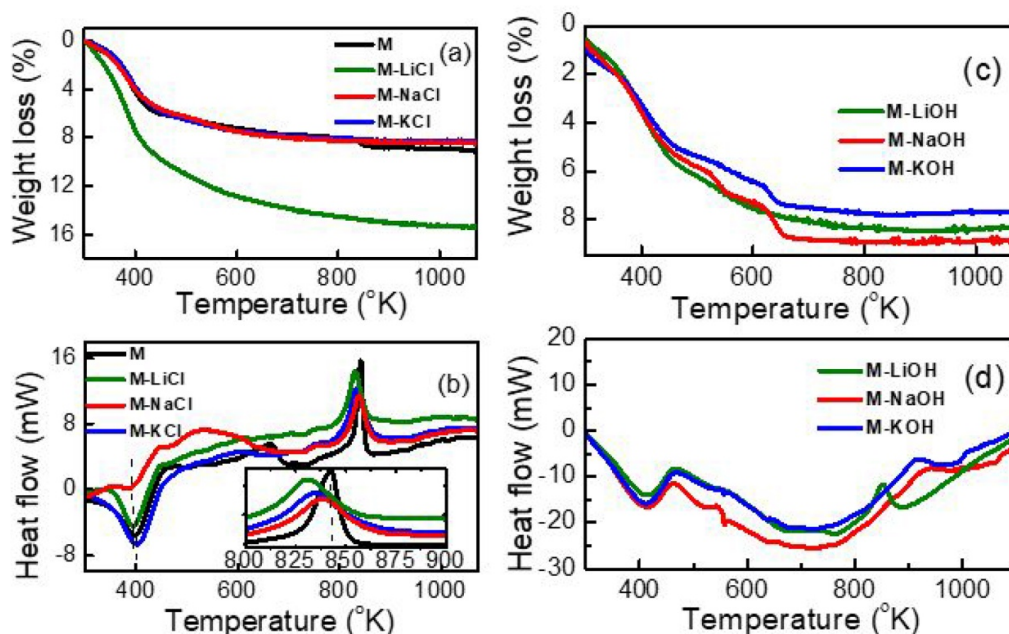
**Figure 5.** The TGA and DTA of bare iron oxide NPs (*M*), *M*–*X*Cl and *M*–*X*OH; *X* = Li, Na, K.

**Table 4.** ICPMS data of *M*–*X*Cl and *M*–*X*OH; *X* = Li, Na, K.

| Sample (0.5 M) | Li-containing ppb | Na-containing ppb | K-containing ppb |
|---|---|---|---|
| *M*–LiCl | 92.7 | — | — |
| *M*–NaCl | — | 62.62 | — |
| *M*–KCl | — | — | 460.7 |
| *M*–LiOH | 70 | — | — |
| *M*–NaOH | — | 525.64 | — |
| *M*–KOH | — | — | 2720.6 |

In addition, the alkali content in *M*–*X*OH is found to be higher than that in *M*–*X*Cl (see table 4). This implies that the diffusion of alkali cations is higher into the lattice along with the adsorption on the surface of NPs incubated in hydroxide solution. The rearrangement of an fcc stacking sequence to an hcp-type stacking sequence of oxygen layers results in a structural transformation from cubic spinel to $\alpha$–Fe$_2$O$_3$ [50, 51]. The introduction of interstitial defects in between the planes hardens the systems, i.e. the motion of stacking faults gets retarded by the interstitial defects [52, 53]. Therefore, the enhanced structural transformation temperature in *M*–*X*–OH may be due to the diffusion of alkali cations in the lattice of magnetite and the occupation of highly vacant interstitial sites.

The ICPMS analysis (see table 4) shows that the number of cations incubated in the alkali chloride solution for the respective cations is found to be lower than that for *M*–*X*OH except for the *M*–LiOH. Despite the lower content of Li in *M*–LiOH than *M*–LiCl, the structural transition temperature for *M*–LiOH is higher. This indicates that the higher stability is due to the occupation of alkali cations in the lattice.

### 3.5. Plausible formation mechanism of modified iron oxide nanoparticles

Based on the above investigations, it is clear that the kinetics of alkali cation incubation on the IONPs is certainly different in chloride and hydroxide media. The plausible mechanism for cation- incubated IONPs and the consequences of heat treatment are depicted in figure 6.

In the case of *M*–*X*Cl, the alkali cations are adsorbed only on the surface of the NPs where they are weakly bonded. Therefore, heat treatment on the *M*–*X*Cl results in the vibrational motion of those adsorbed alkali cations. The motion of the alkali cations initiates the distortion of the iron oxide lattice and lowers the structural transition temperature as indicated by TGA-DTA studies. The alkali adsorbed NPs are also shown to prevent the system from oxidation as shown by the Raman spectra.

When the IONPs are dispersed in an alkaline medium (*M*–*X*OH), the OH$^-$ in the solvent increases the amount of negative charge around the NPs inducing a positive charge on the surface. To maintain charge neutrality, induced negative charges are developed at the centre of the NPs. As a consequence, alkali cations in the solution experience Columbic attraction and succeed in overcoming the surface potential barrier developed by the positive charge on the NPs surface to penetrate the lattice. The depth of penetration may be enhanced by the Columbic attraction force by inducing a negative charge at the centre and the repulsive force by a positive charge on the surface. The cations that diffuse into the lattice
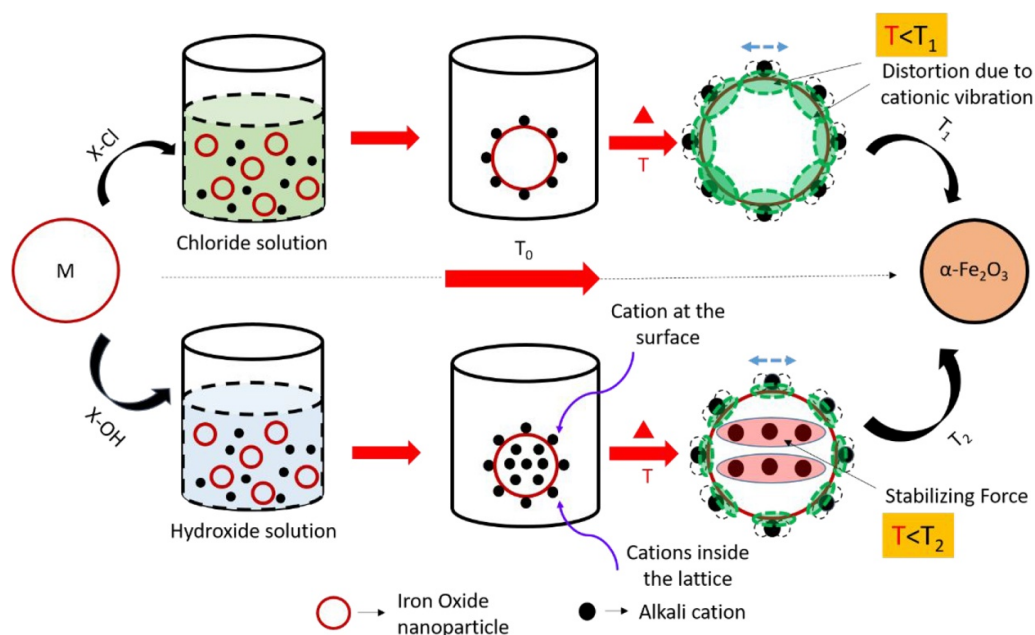
**Figure 6.** A sachematic diagram showing the kinetics of *M*–XCl and *M*–XOH; *X* = Li, Na, K. The increases in the temperature (*T*) vibrate the cations on the surface which distorts the surface atoms resulting in a decrease in the structural transition temperature. The structural transition temperatures are of the order $T_1 < T_0 < T_2$.

of the NPs interlock with the oxygen layers preventing stacking faults in the lattice of cubic iron oxide, thus providing extra stability.

Therefore, the alkali-cation-induced stabilization of the structure results in higher energy for the stacking faults responsible for the structural transition from cubic iron oxide to hematite, which results in an increase of the structural transition temperature of *M*–XOH compared to that of bare IONPs.

### 3.6. Methyl blue decomposition/removal studies

*3.6.1. Effect of cations and functionalizations.* The utilization of IONSs and its composites with carbon for organic dye adsorption is well known [16, 17, 19, 20, 54, 55]. Since the structural, vibrational and magnetic properties are observed to be different for *M*–XCl and *M*–XOH, it is of interest to scrutinize their organic dye absorption/decomposition capability. The negative terminal of MB, i.e. –$SO_3^-$, gets attached to the induced positive charge centres on the surface of the NPs [56]. Therefore, the system with a higher positive charge centre is expected to adsorb higher amounts of MB. The incorporation of alkali cations is proposed to increase the net positive charge of the NPs. Thus the expected increment of the net positive charge is verified by adsorption of the organic dye having a negative terminal.

Hence, MB was considered in this study and the UV absorption of all NPs was measured with respect to time. It is worth mentioning that the main focus of the present research includes understanding and improving the adsorption kinetics of IONPs modified by alkali cations and attached functional groups, although parameters such as the pH of dye solution, initial dye concentrations, adsorbent dosage, temperature, etc,

are important deciding factors for dye adsorption properties. Hence, these deciding parameters are mostly kept constant while exploring the IONPs for MB adsorption.

The capability of IONPs, *M*–XCl and *M*–XOH to adsorb MB dye was evaluated under continuous scanning for a time interval of 50 s by UV–vis spectrometer. The initial MB dye concentration was 50 mg $l^{-1}$ with catalyst loading of 500 mg $l^{-1}$. The concentration of dye was determined by obtaining the absorbance of solution for eight continuous scans using a UV–vis spectrophotometer. The concentration of the MB after adsorption is determined from the standard calibration graph as shown in figure 7(a). The amount of MB adsorbed on the NPs is determined by using the following equation:

$$q_t = [C_0 - C_t]\frac{v}{m} \tag{1}$$

where $q_t$ is the adsorption capacity of MB at time *t*, $C_0$ is the initial concentration of MB, $C_t$ is the concentration of MB at a steady time '*t*' in mg $l^{-1}$, *V* is the volume of MB in l and *m* is the weight of the NPs in g. The adsorption rate is calculated by the following equation,

$$E = \frac{[C_0 - C_t]}{C_0} \times 100\% \tag{2}$$

Figure 7(a) shows the MB absorbance spectra of bare IONPs, *M*–XCl and *M*–XOH. The spectrum was scanned continuously using a UV–vis spectrophotometer and the maximum peak ~600 nm was considered to obtain the amount of MB adsorbed on the NPs. As illustrated in figure 7, there is no significant change in the intensity and absorption maximum of the spectra for *M* and *M*–XCl, which reveals the
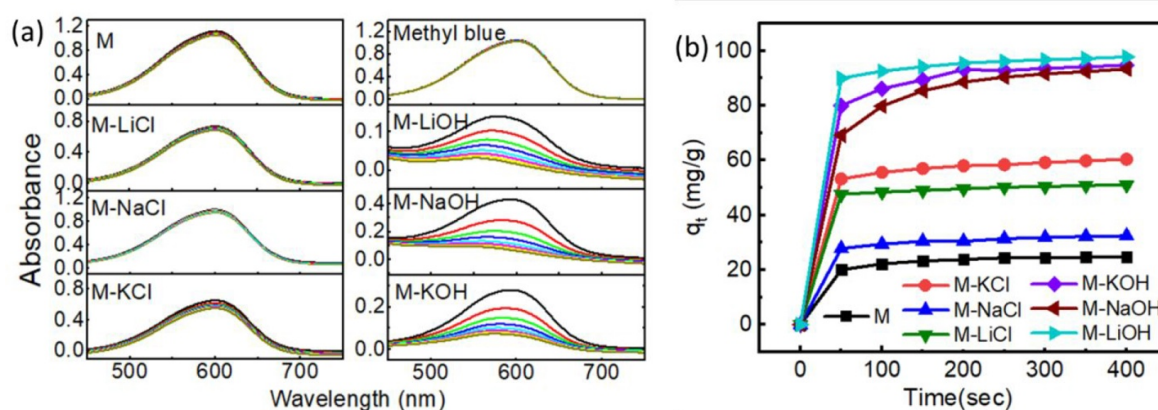
**Figure 7.** (a) The UV–vis absorbance spectra of MB dye in the presence of bare IONPs (*M*), *M*–*X*Cl and *M*–*X*OH. (b) The adsorption of MB by bare IONPs (*M*), *M*–*X*Cl and *M*–*X*OH; *X* = Li, Na, K.

excellent stability of the NPs. A continuous and rapid decrease in absorbance intensity for *M*–*X*OH with time implies the complete decolouration of the MB molecules at a faster rate due to the adsorption of MB dye by alkali-cation-incubated IONPs. As shown in figure 7(b), the process includes rapid MB adsorption within 50 s followed by almost steady adsorption. The first adsorption occurring for the studied IONPs is very quick compared to that of Na-doped g–C$_3$N$_4$ (5 min) [57], Fe$_3$O$_4$@N-doped carbon composite (20 min) [16], Fe$_3$O$_4$ and Fe$_3$O$_4$/reduced graphene oxide (RGO) nanocomposite (40 min) [9], GO (65 min) and RGO (45 min) [10], Fe$_3$O$_4$ and RGO–Fe$_3$O$_4$ (60 min) [19]. Such a rapid MB adsorption reaction by all the IONPs can be attributed to the synergistic effect of both phases, namely maghemite and magnetite, in the structure.

The MB adsorption onto the NPs is studied by plotting a calibration graph of $q_t$ versus time (figure 7(b)). The MB adsorption capacity is found to be enhanced for the alkali-cation-induced and functionalized IONPs. The estimated adsorption capacities of *M, M*–LiCl, *M*–NaCl, and *M*–KCl are found to be 24, 51, 32 and 60 mg g$^{-1}$, respectively (table 5). It is worth mentioning that the highest adsorption capacity by *M*–KCl NPs and the lowest by *M*–NaCl ensures the significant role of cations in the MB adsorption properties. Similar results are reported for the monovalent- and divalent-cation-incorporated GO and RGO nanosheets [10]. This fact correlates to the amount of cations present on the surface of the IONPs, and it is verified from the ICPMS result that the amount of K$^+$ ions is higher and Na$^+$ is lower on the surface of the IONPs in the chloride solution. It has been observed from Mössbauer, Raman, FTIR and TGA-DTA analysis that the alkali cations tailor the net magnetic moment, the vibrational and the structural properties of the IONPs. Moreover, the surface-active property of the nanostructures is a governing factor for the difference in the MB adsorption capacity of *M*–*X*Cl. It has been seen that the ionic polarizability of K$^+$ is higher (0.192 a.u.) than that of Na$^+$ (1.002 a.u.) and Li + (0.192 a.u.) [58]. Thus the higher MB adsorption capacity of *M*–*K*Cl can be attributed to the higher content and

higher ionic polarizability of K$^+$ ions. A much higher MB adsorption capacity of 9 mg g$^{-1}$ is found for *M*–*X*OH, which is comparatively higher than many existing reports (table 5). Higher MB adsorption properties than the present study are also reported in other existing literatures, which can be attained by further tuning the NPs and controlling the process parameters, like the MB concentrations [11, 54]. Hence, improving the performance of NPs further is the focus of our future research. Importantly, present investigations certainly confirm that the presence of OH$^-$ on the IONPs assists in improving the adsorption capacity and establishes an easy interaction with the MB molecules. Although slight changes in the MB adsorption property of *M*–*X*OH are observed, the cationic influences are not significantly noticeable for the first cycle as has been seen in the MB adsorption capacity of *M*–*X*Cl (table 5). A noticeable dependency of cations for the case of *M*–*X*OH is observed when cycles are repeated (see section 3.6.3).

*3.6.2. Adsorption kinetics.* To evaluate the removal/decomposition kinetics of MB by IONPs, pseudo first-order or Lagrangian first-order and second-order kinetic models as well as intra-particle diffusion models are used. The best-fit model is selected based on the linear regression correlation coefficient values ($R^2$). The pseudo-first-order kinetic model is expressed by the following equation [55, 59]:

$$\ln(q_e - q_t) = \ln q_e - k_1 t \tag{3}$$

The pseudo-second-order model is expressed by

$$\frac{t}{q_t} = \frac{1}{k_2 q_e^2} + \frac{t}{q_e} \tag{4}$$

where, $q_t$ and $q_e$ are the MB adsorption capacity (mg g$^{-1}$) at time $t$ and at a steady time, respectively, and $k_1$ and $k_2$ are the respective first and second-order kinetic rate constants (1 s$^{-1}$).

**Table 5.** A comparison table of MB adsorption by various nanomaterials

| Sample | MB concentration | pH | MB adsorption capacity (mg/g) | Ref. |
|---|---|---|---|---|
| Bare IONPs (*M*) | 50 mg/L | 7 | 24.8 | This work |
| *M-Li*OH | | | 97.8 | |
| *M-K*OH | | | 94.8 | |
| *M-Na*OH | | | 93.4 | |
| *M-Li*Cl | | | 51 | |
| *M-Na*Cl | | | 32.4 | |
| *M-K*Cl | | | 60.4 | |
| Neutral chitosan membrane | 60mg/L | 4.5-6.5 | 46.23 | [11] |
| Magnetic chitosan (MC) | | | 60.4 | |
| Graphene oxide (GO) | | | 43.5 | |
| MC-GO | 200 mg/L | | 95.16 | |
| $Fe_3O_4$@N-doped carbon composite | 7.5 mg/L | 11 | 90.84 | [16] |
| Ni-MCM-41 | 50 mg/L | 6.3 | ~38.46 | [56] |

The first-order and pseudo-second-order kinetic plots for MB adsorption onto IONPs are shown in figure 8 and the corresponding parameters are extracted in table 6. From the linear plots in the first-order rate equation, the experimental $q_e$ values are not in good agreement with the calculated ones with a deviation in the range of 18.7%–93.25% and relatively lower determination of the coefficients $R^2$ (0.91187–0.99694) in most cases, which indicates the inapplicability of the first-order kinetic model for the obtained experimental findings.

The fitted data of the pseudo-second-order kinetic model shows a good agreement in terms of higher correlation coefficient values $R^2 \sim 0.99$ and closer values between $q_{e,cal}$ and $q_{e,exp}$ (table 6). Thus, the MB adsorption can be described by the pseudo-second-order rather than the first-order kinetic model, which suggests that chemisorption interaction caused by electrostatic attraction plays a key role in the adsorption process [60]. In addition, the experimentally obtained data are examined by the intra-particle diffusion model to explore further the rate-determining step involved in the MB adsorption. The corresponding Weber and Morris equation is

$$q_t = k_i t^{1/2} + C \qquad (5)$$

where $k_i$ and $C$ are the intra-particle diffusion rate constant and the intercept, respectively. The plot of $q_t$ against $t^{1/2}$ is displayed in figure 8(c) and the corresponding extracted parameters are tabulated in table 6. The slope of such a linear plot determines the rate parameter of intra-particle diffusion, whereas the intercept $C$ is proportional to the boundary layer thickness; the larger the intercept the greater the boundary layer effect. If the plot of $q$ versus $t^{1/2}$ gives a straight line, the adsorption process is controlled by intra-particle diffusion, however, if the data exhibits multi-linear plots, then two or more steps influence the sorption process [61].

The linearized plots are fitted (figure 8(c)) and the corresponding kinetic parameters are calculated (table 6). The correlation coefficient ($R^2$) of this model which is close to unity indicates the possibility of intra-particle diffusion for the dyes adsorbed in a high amount on magnetite NPs. However, the fitted lines do not pass through the origin, which indicates that intra-particle diffusion is not the only rate-determining step in these cases. Some other mechanisms, such as external surface adsorption, may take place simultaneously along with intra-particle diffusion [20, 62].

*3.6.3. Regeneration and reusability of IONPS.* The reusability of NPs is an important factor for ascertaining the adsorption behaviour for practical applications. Since *M–X*OH exhibits promising MB adsorption properties compared to the *M–X*Cl counterpart, a reusability study is only carried out for the *M–X*OH. The reusability of *M–X*OH towards MB dye molecule adsorption was studied repeatedly for eight to nine cycles using a UV–vis spectrometer (see figure 9(a)) depending upon how much the NPs could adsorb the dye, i.e. till saturation of the NPs. Each cycle consists of eight continuous scans and the value of maximum adsorption is considered. Figure 9(a) displays the reusability of *M–X*OH for MB adsorption. The main noticeable features obtained from figure 9(a) are as follows: (i) *M–K*OH is mostly capable of maximum MB adsorption in each cycle, and (ii) it does not attain saturation at nine cycles, whereas *M–*LiOH and *M–*NaOH take eight cycles. To extend reusability further, saturated *M–K*OH is collected and incubated again in an alkali hydroxide medium for two days. These incubated NPs are thereafter washed and dried (*M–K*OH$_s$) to retest the adsorption of dye molecules. The MB adsorption result of *M–X*OH$_s$, as shown in figure 9(b), reveals the potentiality of reusing $K^+$-ion-induced and OH-functionalized IONPs.

*3.6.4. Plausible mechanism of MB adsorption.* Physical insights from the aforementioned results are explored with the help of ATR-FTIR spectroscopy. The FTIR spectra of all IONPs were recorded before and after the adsorption of MB dye (see figures 2 and 10) to understand the mechanism of adsorption. Figure 10 shows the FTIR spectra of incubated NPs after MB adsorption. The peak at 3530 cm$^{-1}$ is due to N–H stretching. The band at 3145 cm$^{-1}$ is assigned to C–H stretching vibrations. Two peaks at 1500 and 1576 cm$^{-1}$ are

**Table 6.** Adsorption kinetics parameters of MB of bare iron oxide NPs (*M*), *M*–XCl and *M*–XOH; *X* = Li, Na, K.

| Samples | $q_{e,expt}$ (mg g$^{-1}$) | First-order kinetics | | | Second-order kinetics | | | Intra-particle diffusion | | |
|---|---|---|---|---|---|---|---|---|---|---|
| | | $K_1$ | $R^2$ | $q_{e,cal}$ | (mg g$^{-1}$) | $K_2$ | $R^2$ | $q_{e,cal}$ (mg g$^{-1}$) | $K_i$ (mg g$^{-1}$ min$^{1/2}$) |
| *M* | 24.8 | 0.01047 | 0.976 | 7.6 | 0.003 | 0.999 | 25.0 | 0.34 | 18.43 | 0.87 |
| *M*–LiCl | 51 | 0.00843 | 0.997 | 12.32 | 0.004 | 0.999 | 52.6 | 0.27 | 45.72 | 0.99 |
| *M*–NaCl | 32 | 0.01042 | 0.999 | 39.37 | 0.002 | 0.999 | 33.3 | 0.35 | 25.73 | 0.96 |
| *M*–KCl | 60.4 | 0.01039 | 0.937 | 22.89 | 0.001 | 0.999 | 62.5 | 0.53 | 50.06 | 0.97 |
| *M*–LiOH | 97.8 | 0.00882 | 0.927 | 6.6 | 0.002 | 0.999 | 99.1 | 0.59 | 86.60 | 0.96 |
| *M*–NaOH | 93.4 | 0.00951 | 0.912 | 8.78 | 0.001 | 0.999 | 98.4 | 1.74 | 61.24 | 0.88 |
| *M*–KOH | 94.8 | 0.00768 | 0.969 | 10.97 | 0.001 | 0.999 | 97.6 | 1.10 | 74.8 | 0.86 |
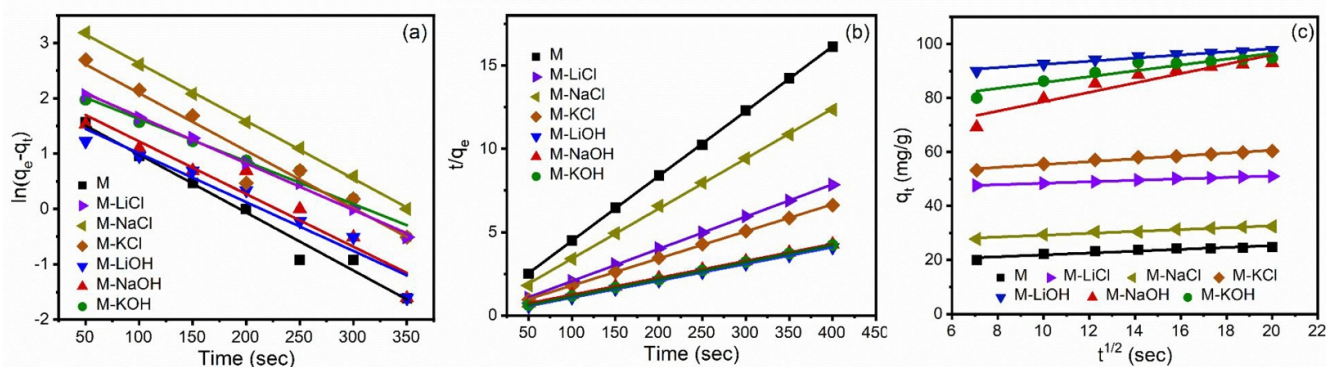


**Figure 8.** (a) First-order kinetics, (b) second-order kinetics and (c) diffusion kinetics for adsorption of MB of bare iron oxide NPs (*M*), *M*–XCl and *M*–XOH; *X* = Li, Na, K.
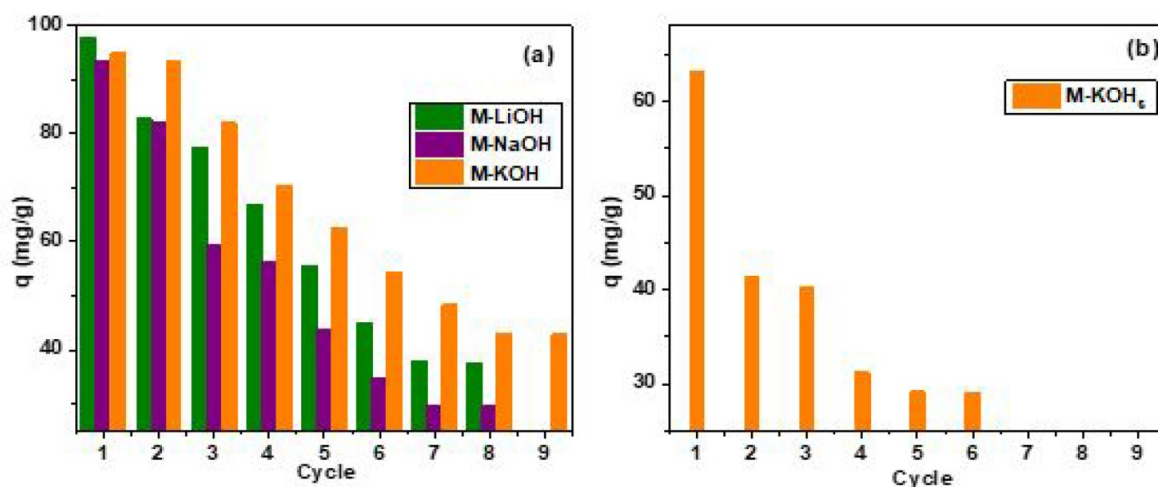


**Figure 9.** A reusability study for the adsorption of MB onto *M*–XOH (where *X* = Li, Na, K). (a) The adsorption effect of the nanoparticles incubated in alkali hydroxide and (b) saturated *M*–KOH (*M*–KOH$_s$).

attributed to the stretching of (C = N) and (C = C), respectively. The other two bands at 1158 and 1345 cm$^{-1}$ correspond to the stretching of (S = O) [19].

Prominent peaks of MB are obtained around 1170 and 1345 cm$^{-1}$ which corresponds to the stretching of (S = O), and 1505 cm$^{-1}$ which corresponds to the stretching of (C–N) [10]. The FTIR spectra of the alkali chloride show weak peaks corresponding to MB for *M*–XCl (figure 10(a)) whereas no adsorption peak related to MB is noticed from *M*–XOH (figure 10(b)). This observation indicates that the surface adsorption

of MB takes place for *M*–XCl, whereas MB is decomposed in *M*–X–OH. In addition, the concentration of the MB in *M*–XOH is drastically reduced with time. This may be attributed to the decomposition of MB along with adsorption. Decomposition is only plausible when the OH$^-$ functional groups present are weakly bonded to the surface of the NPs. The OH$^-$ reacts efficiently with the MB resulting in its decomposition.

To verify the presence of –OH$^-$ functional groups on the surface, the NPs incubated in the alkali hydroxide were dispersed in dilute HCl for 1 min, and the activity
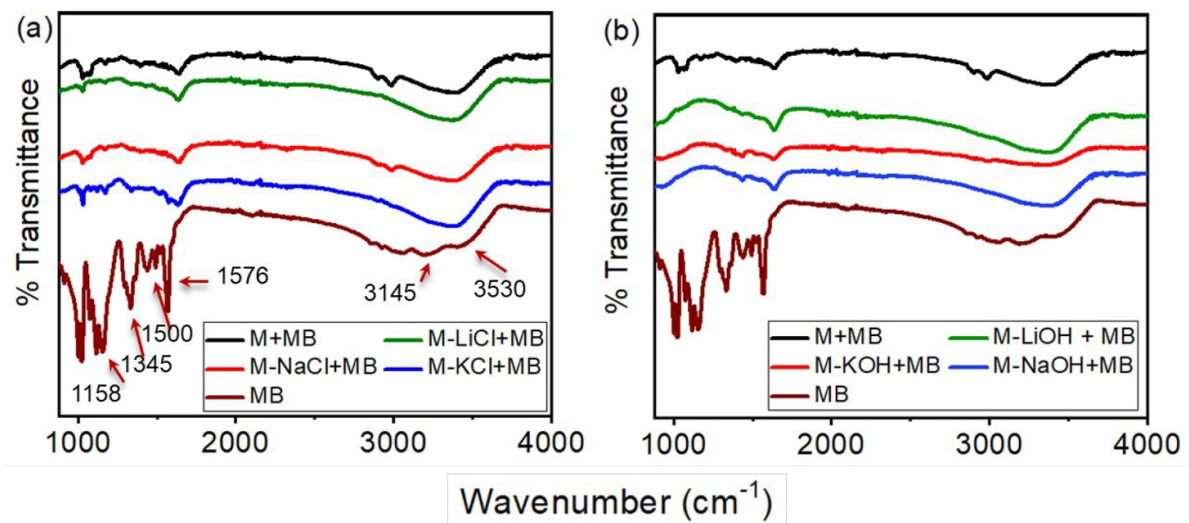
**Figure 10.** The FTIR spectra of (a) *M*–*X*Cl and (b) *M*–*X*OH after adsorption of MB; *X* = Li, Na, K.
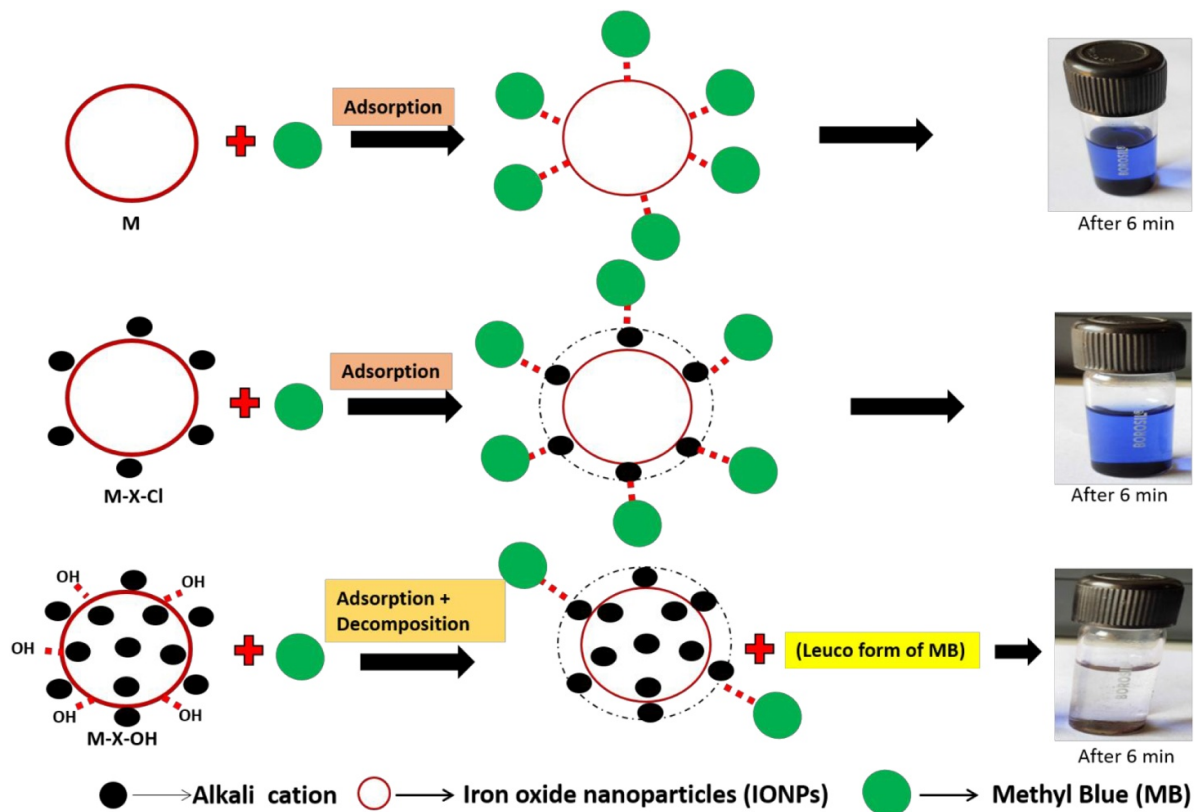


**Figure 11.** A schematic diagram of the decomposition and adsorption of MB by bare and modified IONPs.

was then measured. The acid medium neutralizes the surface, which removes the –OH resulting in an immense reduction in activity. The resultant NPs are found to be inactive in the MB decomposition. Moreover, the saturated *M*–*X*OH was incubated again in the alkali hydroxides and found to recover promisingly, decolourising the MB further. It is worth mentioning that MB adsorption by *M*–*X*Cl is a very lengthy process in which

decolourization takes 5–6 h to complete, whereas MB decomposition in *M*–*X*–OH is very fast. These facts signify the importance of OH$^-$ functional groups on the IONPs for MB to decompose effectively.

To validate the concept of MB decomposition in *M*–*X*OH, MB was added to the basic solution and obvious decolourization was found to take place. Moreover, the use of an alkaline medium is harmful to the ecosystem [63] and

the use of $OH^-$ functionalized IONPs is safe and effective for MB decomposition. The MB is adsorbed on the surface of *M*–*X*Cl which is in agreement with the FTIR spectra, as shown in figure 10(a). The adsorption of MB is attributed to the strong electrostatic interaction between the cation-rich positive site of modified IONPs and the negative functional group ($SO_3^-$) of MB [56]. A schematic of adsorption and decomposition is shown in figure 11. The higher MB adsorption capability of *M*–*X*OH compared to *M*–*X*Cl is due to the greater content of alkali cations with the higher polarizability on those IONPs. The $OH^-$ group present in *M*–*X*OH can be attached to the nitrogen groups of the MB molecule to form an intermolecular hydrogen bond [64]. Moreover, the reaction of *M*–*X*OH with MB dye may lead to intermediates or a leuco form of the compound which maintain an aromatic structure. The $OH^-$ group has a reaction ability high enough to attack any organic molecule. It may also exhibit fluorescence even if the chromogenic structure is altered or destroyed. Further reactions may lead to smaller organic molecules [65]. Thus, decomposition of MB dye takes place along with adsorption for *M*–*X*OH.

## 4. Conclusion

Alkali-decorated and functionalized iron oxide nanoparticles (IONPs) were synthesized by a simple and inexpensive co-precipitation method. The as-synthesized IONPs reveal the presence of both phases of cubic iron oxide: maghemite and magnetite. The relative amount between these two phases, the thermal properties, magnetic properties and structural stability of the IONPs are demonstrated to be tailored by incorporating alkali cations into the IO matrix. Distinct modified IONP features are obtained depending on the incubation environment: (i) IONPs incubated in alkali hydroxide were found to have higher structural transition temperatures, which is attributed to the diffusion of cations into the lattices of nanoparticles; (ii) a reduction in the mean hyperfine field of NPs dispersed in alkali hydroxide associated with a reduction in the net magnetic moment of the NPs; (iii) only adsorption of MB takes places for IONPs incubated in alkali chloride, whereas the decomposition and adsorption of MB occurs by the IONPs incubated in alkali hydroxide.

The higher adsorption capability of IONPs incubated in alkali hydroxide is attributed to the short-range diffusion of dye molecules in the structure and easy interaction with the dye molecules. Moreover, the higher MB adsorption capacity of $K^+$-ion-incubated IONPs is ascribed to the higher cation content and higher atomic polarizability. Finally, $K^+$-ion-incubated IONPs with $OH^-$ functionalization are easier to prepare, more cost-effective and more efficient in removing MB from an aqueous solution than other alkali-cation-incorporated IONPs and functionalities.

## Author contributions

N J S carried out the experiment, the analyzed data and wrote the manuscript; B W assisted in analysis and writing; B P S and S S P did the TEM; P K A carried out TGA-DTA; H P S carried out ICPMS; S C did the Raman spectroscopy; A C O and V K G conducted the Mössbauer spectroscopy; S G and L H S planned, conceptualized, supervised and wrote the manuscript; S B reviewed and edited the manuscript. All authors discussed the results, commented on the manuscript, and gave approval to the final version of the manuscript.

## ORCID iDs

Subrata Ghosh https://orcid.org/0000-0002-5189-7853
Suelen Barg https://orcid.org/0000-0002-0723-7081

## References

[1] Ahmed S N and Haider W 2018 Heterogeneous photocatalysis and its potential applications in water and wastewater treatment: a review *Nanotechnology* **29** 342001

[2] Chowdhary P, Raj A and Bharagava R N 2018 Environmental pollution and health hazards from distillery wastewater and treatment approaches to combat the environmental threats: a review *Chemosphere* **194** 229–46

[3] Norvill Z N, Shilton A and Guieysse B 2016 Emerging contaminant degradation and removal in algal wastewater treatment ponds: identifying the research gaps *J. Hazard. Mater.* **313** 291–309

[4] Zhan B J, Li J S, Xuan D X and Poon C S 2020 Recycling hazardous textile effluent sludge in cement-based construction materials: physicochemical interactions between sludge and cement *J. Hazard. Mater.* **381** 121034

[5] Thy L T M, Thuong N H, Tu T H, Nam H M, Hieu N H and Phong M T 2019 Synthesis of magnetic iron oxide/graphene oxide nanocomposites for removal of cadmium ions from water *Adv. Nat. Sci. Nanosci. Nanotechnol.* **10** 025006

[6] Malik A, Rahman M, Ansari M I, Masood F and Grohmann E 2012 Environmental protection strategies: an overview In: Malik A, Grohmann E *Environmental Protection Strategies for Sustainable Development* (Springer: Berlin) pp 1–34

[7] Li Y, Luo Y and He Q 2020 Chemical footprint of textile and apparel products: an assessment of human and ecological toxicities based on USEtox model *J. Text. Inst.* **5000** 1–12

[8] Khan S T and Malik A 2019 Engineered nanomaterials for water decontamination and purification: from lab to products *J. Hazard. Mater.* **363** 295–308

[9] Minitha C R, Martina Susan Arachy M and Rajendra Kumar R T 2018 Influence of $Fe_3O_4$ nanoparticles decoration on dye adsorption and magnetic separation properties of $Fe_3O_4$/rGO nanocomposites *Sep. Sci. Technol.* **53** 2159–69

[10] Sharma P, Hussain N, Borah D J and Das M R 2013 Kinetics and adsorption behavior of the methyl blue at the graphene oxide/reduced graphene oxide nanosheet–water interface: a comparative study *J. Chem. Eng. Data* **58** 3477–88

[11] Fan L, Luo C, Li X, Lu F, Qiu H and Sun M 2012 Fabrication of novel magnetic chitosan grafted with graphene oxide to enhance adsorption properties for methyl blue *J. Hazard. Mater.* **215–6** 272–9

[12] Gu X, Li C, Yuan S, Ma M, Qiang Y and Zhu J 2016 ZnO based heterojunctions and their application in environmental photocatalysis *Nanotechnology* **27** 1–21

[13] He X, Wang J, Shu Z, Tang A and Yang H 2016 $Y_2O_3$ functionalized natural palygorskite as an adsorbent for methyl blue removal *RSC Adv.* **6** 41765–71

[14] Li L H, Xiao J, Liu P and Yang G W 2015 Super adsorption capability from amorphousization of metal oxide nanoparticles for dye removal *Sci. Rep.* **5** 9028

[15] Sun Q, Wu K, Zhang J and Sheng J 2019 Construction of $ZnFe_2O_4$/rGO composites as selective magnetically recyclable photocatalysts under visible light irradiation *Nanotechnology* **30** 315706

[16] Tadesse A, RamaDevi D, Hagos M, Battu G and Basavaiah K 2018 Synthesis of nitrogen doped carbon quantum dots/magnetite nanocomposites for efficient removal of methyl blue dye pollutant from contaminated water *RSC Adv.* **8** 8528–36

[17] Kouhbanani M A J, Beheshtkhoo N, Taghizadeh S, Amani A M and Alimardani V 2019 One-step green synthesis and characterization of iron oxide nanoparticles using aqueous leaf extract of Teucrium polium and their catalytic application in dye degradation *Adv. Nat. Sci. Nanosci. Nanotechnol.* **10** 015007

[18] Ali A, Zafar H, Zia M, Ul Haq I, Phull A R, Ali J S and Hussain A 2016 Synthesis, characterization, applications, and challenges of iron oxide nanoparticles *Nanotechnol. Sci. Appl.* **9** 49–67

[19] Boruah P K, Borah D J, Handique J, Sharma P, Sengupta P and Das M R 2015 Facile synthesis and characterization of $Fe_3O_4$ nanopowder and $Fe_3O_4$/reduced graphene oxide nanocomposite for methyl blue adsorption: A comparative study *J. Environ. Chem. Eng.* **3** 1974–85

[20] Saha B, Das S, Saikia J and Das G 2011 Preferential and enhanced adsorption of different dyes on iron oxide nanoparticles: a comparative study *J. Phys. Chem.* C **115** 8024–33

[21] Wu W, Wu Z, Yu T, Jiang C and Kim W-S 2015 Recent progress on magnetic iron oxide nanoparticles: synthesis, surface functional strategies and biomedical applications *Sci. Technol. Adv. Mater.* **16** 023501

[22] Wu M, Zhang D, Zeng Y, Wu L, Liu X and Liu J 2015 Nanocluster of superparamagnetic iron oxide nanoparticles coated with poly (dopamine) for magnetic field-targeting, highly sensitive MRI and photothermal cancer therapy *Nanotechnology* **26** 115102

[23] Tong S, Quinto C A, Zhang L, Mohindra P and Bao G 2017 Size-dependent heating of magnetic iron oxide nanoparticles *ACS Nano* **11** 6808–16

[24] Jarrett B R, Frendo M, Vogan J and Louie A Y 2007 Size-controlled synthesis of dextran sulfate coated iron oxide nanoparticles for magnetic resonance imaging *Nanotechnology* **18** 035603

[25] Parkinson G S 2016 Iron oxide surfaces *Surf. Sci. Rep.* **71** 272–365

[26] Márquez F, Campo T, Cotto M, Polanco R, Roque R, Fierro P, J M S, Elizalde E and Morant C 2011 Synthesis and characterization of monodisperse magnetite hollow microspheres *Soft Nanosci. Lett.* **01** 25–32

[27] Lazarevic Z Z, Jovalekic C, Sekulic D, Slankamenac M, Romcevic M, Milutinovic A and Romcevic N Z 2012 Characterization of nanostructured spinel NiFe2O4 obtained by soft mechanochemical synthesis *Sci. Sinter.* **44** 331–9

[28] Pal U, Sandoval A, Madrid S I U, Corro G, Sharma V and Mohanty P 2016 Mixed titanium, silicon, and aluminum oxide nanostructures as novel adsorbent for removal of rhodamine 6G and methylene blue as cationic dyes from aqueous solution *Chemosphere* **163** 142–52

[29] Gnanaprakash G, Ayyappan S, Jayakumar T, Philip J and Raj B 2006 Magnetic nanoparticles with enhanced $\gamma$-$Fe_2O_3$ to $\alpha$-$Fe_2O_3$ phase transition temperature *Nanotechnology* **17** 5851–7

[30] El-Shobaky G A and Ibrahim A A 1987 Solid-solid interactions between ferric oxide and lithium carbonate and the thermal stability of the lithium ferrites produced *Thermochim. Acta* **118** 151–8

[31] Chen J and Chen H 2018 Removal of anionic dyes from an aqueous solution by a magnetic cationic adsorbent modified with DMDAAC *New J. Chem.* **42** 7262–71

[32] Goss C 1988 Saturation magnetisation, coercivity and lattice parameter changes in the system Fe3O4-?Fe2O3, and their relationship to structure *Phys. Chem. Miner.* **16** 164–71

[33] Mahdavi M, Ahmad M B, Haron M J, Gharayebi Y, Shameli K and Nadi B 2013 Fabrication and characterization of SiO2/(3-aminopropyl)triethoxysilane-coated magnetite nanoparticles for lead(II) removal from aqueous solution *J. Inorg. Organomet. Polym. Mater.* **23** 599–607

[34] Baltrusaitis J, Schuttlefield J, Zeitler E and Grassian V H 2011 Carbon dioxide adsorption on oxide nanoparticle surfaces *Chem. Eng. J.* **170** 471–81

[35] Jubb A M and Allen H C 2010 Vibrational spectroscopic characterization of hematite, maghemite, and magnetite thin films produced by vapor deposition *ACS Appl. Mater. Interfaces* **2** 2804–12

[36] Shebanova O N and Lazor P 2003 Raman spectroscopic study of magnetite (FeFe2O4): a new assignment for the vibrational spectrum *J. Solid State Chem.* **174** 424–30

[37] de Faria D L A, Venâncio Silva S and de Oliveira M T 1997 Raman microspectroscopy of some iron oxides and oxyhydroxides *J. Raman Spectrosc.* **28** 873–8

[38] Ghosh S, Polaki S R, Sahoo G, Jin E-M, Kamruddin M, Cho J S and Jeong S M 2019 Designing metal oxide-vertical graphene nanosheets structures for 2.6 V aqueous asymmetric electrochemical capacitor *J. Ind. Eng. Chem.* **72** 107–16

[39] Hanesch M 2009 Raman spectroscopy of iron oxides and (oxy)hydroxides at low laser power and possible applications in environmental magnetic studies *Geophys. J. Int.* **177** 941–8

[40] Testa-Anta M, Ramos-Docampo M A, Comesaña-Hermo M, Rivas-Murias B and Salgueiriño V 2019 Raman spectroscopy to unravel the magnetic properties of iron oxide nanocrystals for bio-related applications *Nanoscale Adv.* **1** 2086–103

[41] da Silva S W *et al* 2017 Mössbauer and Raman spectroscopic study of oxidation and reduction of iron oxide nanoparticles promoted by various carboxylic acid layers *J. Radioanal. Nucl. Chem.* **312** 111–9

[42] Ghosh S, Polaki S R, Ajikumar P K, Krishna N G and Kamruddin M 2018 Aging effects on vertical graphene

nanosheets and their thermal stability *Indian J. Phys.* **92** 337–42

[43] El Mendili Y, Bardeau J-F, Randrianantoandro N, Gourbil A, Greneche J-M, Mercier A-M and Grasset F 2011 New evidences of in situ laser irradiation effects on γ-Fe2O3 nanoparticles: a Raman spectroscopic study *J. Raman Spectrosc.* **42** 239–42

[44] Soler M A G, Challa, S S R, Kumar and Qu F 2012 Raman spectroscopy of iron oxide nanoparticles *Raman Spectroscopy for Nanomaterials Characterization* vol 9783642206 (Berlin Heidelberg: Springer) pp 379–416

[45] Herojit Singh L, Govindaraj R, Amarendra G and Sundar C S 2013 Local structure and magnetic properties of cubic iron oxide nanoparticles formed in zeolite as deduced using Mössbauer spectroscopy *Appl. Phys. Lett.* **103** 193104

[46] Herojit Singh L, Panda A, Govindaraj R, Mythili R and Amarendra G 2018 Implications of linear correlation between hyperfine parameters in iron oxide nanoparticles *Mater. Chem. Phys.* **214** 440–8

[47] Sousa E C, Rechenberg H R, Depeyrot J, Gomes J A, Aquino R, Tourinho F A, Dupuis V and Perzynski R 2009 In-field Mossbauer study of disordered surface spins in core/shell ferrite nanoparticles *J. Appl. Phys.* **106** 0–7

[48] Kuhn L T, Bojesen A, Timmermann L, Nielsen M M and M Rup S 2002 Structural and magnetic properties of core shell iron iron oxide nanoparticles *J. Phys. Condens. Matter* **14** 13551–67

[49] Zhang L, He R and Gu H 2006 Oleic acid coating on the monodisperse magnetite nanoparticles *Appl. Surf. Sci.* **253** 2611–7

[50] Singh L H, Govindaraj R, Mythili R, Amarendra G and Sundar C S 2013 Atomic scale study of thermal reduction of nano goethite coexisting with magnetite *AIP Adv.* **3** 022101

[51] Watanabe Y and Ishii K 1995 Geometrical consideration of the crystallography of the transformation from α-Fe2O3 to Fe3O4 *Phys. Status Solidi* **150** 673–86

[52] Guiu F 1969 The influence of lattice friction on point defect hardening *Philos. Mag.* **20** 51–66

[53] Zbib H M, Díaz de la Rubia T, Rhee M and Hirth J P 2000 3D dislocation dynamics: stress–strain behavior and hardening mechanisms in fcc and bcc metals *J. Nucl. Mater.* **276** 154–65

[54] Sharma S, Hasan A, Kumar N and Pandey L M 2018 Removal of methylene blue dye from aqueous solution using immobilized Agrobacterium fabrum biomass along with

iron oxide nanoparticles as biosorbent *Environ. Sci. Pollut. Res.* **25** 21605–15

[55] Ruíz-Baltazar Á D J, Reyes-López S Y, Mondragón-Sánchez M D L, Robles-Cortés A I and Pérez R 2019 Eco-friendly synthesis of Fe3O4 nanoparticles: evaluation of their catalytic activity in methylene blue degradation by kinetic adsorption models *Results Phys.* **12** 989–95

[56] Shu Y, Shao Y, Wei X, Wang X, Sun Q, Zhang Q and Li L 2015 Synthesis and characterization of Ni-MCM-41 for methyl blue adsorption *Microporous Mesoporous Mater.* **214** 88–94

[57] Fronczak M, Krajewska M, Demby K and Bystrzejewski M 2017 Extraordinary adsorption of methyl blue onto sodium-doped graphitic carbon nitride *J. Phys. Chem.* C **121** 15756–66

[58] Pyper N C, Pike C G and Edwards P P 1992 The polarizabilities of species present in ionic solutions *Mol. Phys.* **76** 353–72

[59] Zhang H, Chang Q, Jiang Y, Li H and Yang Y 2018 Synthesis of KMnO 4 -treated magnetic graphene oxide nanocomposite (Fe 3 O 4 @GO/MnO x) and its application for removing of Cu 2+ ions from aqueous solution *Nanotechnology* **29** 135706

[60] An Y, Zheng H, Yu Z, Sun Y, Wang Y, Zhao C and Ding W 2020 Functioned hollow glass microsphere as a self-floating adsorbent: rapid and high-efficient removal of anionic dye *J. Hazard. Mater.* **381** 120971

[61] Alver E and Metin A Ü 2012 Anionic dye removal from aqueous solutions using modified zeolite: adsorption kinetics and isotherm studies *Chem. Eng. J.* **200–202** 59–67

[62] Doğan M, Alkan M, Türkyilmaz A and Özdemir Y 2004 Kinetics and mechanism of removal of methylene blue by adsorption onto perlite *J. Hazard. Mater.* **109** 141–8

[63] Gomes H I, Mayes W M, Rogerson M, Stewart D I and Burked I T 2016 Alkaline residues and the environment: A review of impacts, management practices and opportunities *J. Clean. Prod.* **112** 3571–82

[64] Mohamed R M, Shawky A and Mkhalid I A 2017 Facile synthesis of MgO and Ni-MgO nanostructures with enhanced adsorption of methyl blue dye *J. Phys. Chem. Solids* **101** 50–57

[65] Colonna G M, Caronna T and Marcandalli B 1999 Oxidative degradation of dyes by ultraviolet radiation in the presence of hydrogen peroxide *Dye. Pigment.* **41** 211–20